Liquid-feed flame spray pyrolysis as alternative synthesis for electrochemically active nano-sized Li_2MnSiO_4

2016 Transl. Mater. Res. 3 025001

(http://iopscience.iop.org/2053-1613/3/2/025001)

Translational Materials Research

OPEN ACCESS

RECEIVED
17 December 2015

REVISED
19 February 2016

ACCEPTED FOR PUBLICATION
24 March 2016

PUBLISHED
5 May 2016

PAPER

Liquid-feed flame spray pyrolysis as alternative synthesis for electrochemically active nano-sized Li_2MnSiO_4

Nils Wagner, Ann Mari Svensson and Fride Vullum-Bruer

Department of Materials Science and Engineering, Norwegian University of Science and Technology, 7491 Trondheim, Norway

E-mail: fride.vullum-bruer@ntnu.no

Keywords: Li-ion batteries, Li_2MnSiO_4, flame spray pyrolysis, scalable synthesis, high capacity

Supplementary material for this article is available online

Abstract

A novel liquid-feed flame spray pyrolysis synthesis with reducing post-heat treatment yielding highly phase pure nano-sized and carbon-coated Li_2MnSiO_4 is reported. In contrast to most reported Li_2MnSiO_4 synthesis routes, aerosol combustion methods are highly scalable and not as time consuming as most wet chemical syntheses. Flame spray pyrolysis was performed using solutions with varying ratios of H_2O, EtOH and p-Xylene. The importance of solution combustibility to form loosely agglomerated nanoparticles is highlighted. Particles from the p-Xylene-aided flame spray pyrolysis showed a mean particle size of 20 nm and $Pmn2_1$ structure after annealing and carbon coating. The electrochemical performance as a cathode material was assessed by galvanostatic cycling and *in situ* XRD in half cells. The highest discharge capacity observed was 190 mAh g^{-1} at room temperature and a rate of C/50.

Introduction

At present, rechargeable Li-ion batteries outperform all other battery concepts with respect to volumetric and gravimetric energy density. Nonetheless, extensive research is on-going to optimise the cells. In particular, the positive electrode materials show a great mismatch in specific capacity compared to graphite which is used as negative electrode in commercially available Li-ion batteries [1]. Moreover, the most common cathode material in Li-ion batteries, $LiCoO_2$, accounted for about 50% of the materials cost of the battery by the year 2000 [2]. A more recent study using NMC shows the cathode side being responsible for 32–47% of the cost per Ah [3]. Lately, polyanion materials like phosphates and silicates based on the abundant elements Fe and Mn as redox active ions gained attention and represent with Li_2MnSiO_4 (LMS) a material which in theory can deliver 2 Li ions per formula unit and thus in theory offer capacities exceeding 300 mAh g^{-1} [4–7]. In fact, according to a recent study by Andre *et al* from the BMW group, LMS would theoretically meet the required energy density and capacity values for the next generation Li-ion battery cathodes in all-electric vehicles [8]. Dominko *et al* first reported LMS as a potential cathode for Li-ion batteries in 2006 and indexed it to the tetrahedral structures with the orthorhombic space-group $Pmn2_1$ [6, 9]. Afterwards, another orthorhombic and two monoclinic polymorphs, namely *Pmnb*, $P2_1n$ and *Pn*, all adopting Li_3PO_4 structures, were reported [10–12]. Just like the Fe analogue, Li_2FeSiO_4, LMS is a poor electronic and ionic conductor and thus requires nanoscale particles and a conductive coating to overcome these shortcomings [6, 13, 14]. However, it is believed that changes in the Mn coordination during oxidation cause amorphisation of the structure which leads to irreversible capacity fading [15–18]. *Ab initio* calculations by Saracibar *et al* predict that Ni substitution could be beneficial to stabilise the crystal structure upon delithiation (oxidation) [16]. The vast majority of reported syntheses of LMS are wet chemical methods. Solvothermal syntheses deliver the highest reported capacities of over 200 mAh g^{-1} in the first discharge [19–22]. Other authors report success by sol–gel related methods, polyol methods or molten carbonate syntheses [23–27]. However, these wet-chemical routes can be very time consuming. Sol–gel syntheses with a process time of up to 8 d are reported [23]. Another major drawback of wet chemical syntheses is the limited scalability. If a new cathode material shall ever be commercialised, scalability and time efficiency are very important factors. Flame assisted

aerosol processes like flame hydrolysis and flame spray pyrolysis combine scalability and time efficiency while allowing good control of particle sizes in the nano-regime. Nano-sized fumed silica, titania and carbon blacks are in fact commercially produced in large quantities by aerosol flame processes [28]. Here we report production of LMS by an alternative novel synthesis route, namely liquid-feed flame spray pyrolysis (FSP), combined with a reducing heat treatment and carbon coating as an excellent scalable and time-efficient route to obtain nano-sized LMS. We especially highlight the importance of solution combustibility towards the morphology and thus the electrochemical performance of the final product. In addition, influences on XRD phase purity dependent on Mn stoichiometry are discussed and the structural degradation is investigated by *in situ* XRD during galvanostatic cycling.

Experiment

Sample preparation

Two different kinds of precursor solution for FSP were investigated. The first approach was a solution based on a water-to-EtOH ratio of 1:5 by volume. 0.06 mole dried $LiNO_3$ (Alfa Aesar, 99%) and 0.03 mole $Mn(NO_3)_2 \bullet 4H_2O$ (Merck Ensure for analysis, >98%) were dissolved in 20 ml deionised H_2O and added to a solution of 0.03 mole tetraethyl orthosilicate (TEOS) (VWR 99%) in 80 ml EtOH under vigorous stirring. In the second approach the solution was based on a p-Xylene-to-EtOH ratio of 1:5 by volume. The same Li, Mn and Si precursors were dissolved in 100 ml EtOH at 50 °C under vigorous stirring and prior to pyrolysis 25 ml p-Xylene was added as a fuel enhancer. Following this route, samples with 6 and 9 mole% Mn sub-stoichiometry were also produced. FSP was performed on a NPS10, Tethis S.p.A. The solutions were sprayed into a CH_4/O_2 (flow rate: 1.5/3 l min^{-1}) flame at a constant liquid and dispersion gas (O_2) flow rate of 5 ml min^{-1}. The pressure drop (dispersion gas at the nozzle tip) was set to ~2.0 bar and the powders were collected on a glass microfiber filter (Whatman GF6). After FSP the as-pyrolysed precursors were mixed with 25 wt.% corn-starch (Carl Roth GmbH & Co. KG for laboratory use) and wet ball milled for 10 h using YSZ grinding balls (Ø 5 mm) and EtOH as a dispersant in a 125 ml polyethylene bottle. As a final step the precursor mixtures were heat treated in a reducing atmosphere (5% H_2 in Ar: flow rate 25 l h^{-1}) at three different temperatures, 550, 600 and 650 °C and different dwell times. The heating and cooling rate was in all cases 200 °C h^{-1}. The final heat treatment parameters were 650 °C for 10 h in all cases. For clarity reasons a sample index comprising the differences of the synthesised samples is given in table 1.

For cathode preparation a slurry containing 75 wt.% active material, 15 wt.% conductive carbon (Super P Timcal) and 10 wt.% polyvinylidene fluoride (PVDF) (Kynar, reagent grade) as binder dispersed in N-Methyl-2-pyrrolidone (NMP) (Sigma Aldrich >99%) was prepared and tape cast on Al foil as a current collector and dried for 12 h at 90 °C in a vacuum oven. The solid load was about 1 mg cm^{-2}.

Characterisation

Phase formation and structural analysis of the samples was performed by x-ray powder diffraction. XRD patterns were recorded on a Bruker D 8 Advance Da-Vinci, equipped with a linear PSD detector working in Bragg–Brentano (Θ/2Θ) geometry. All powder patterns were recorded using Cu K_α radiation (1.540 60 Å). Patterns for phase formation analysis were recorded from 15 to 75° 2Θ with a step-size of 0.013 ° and an integration time of 0.75 s. For structural analysis, patterns were recorded from 15 to 140° 2Θ with a step-size of 0.013° and an integration time of 1 s. Structural refinements were performed with Topas (Bruker AXS Version 4.2). A Pearson approximation (PVII) was applied to refine the peak shapes. All atomic positions not fixed by $Pmn2_1$ geometry were allowed to converge, starting with the heaviest element. Refinements were also used to quantify the phase fraction of powder diffraction patterns. Details about *in situ* XRD measurements are given in the next paragraph. The surface area and pore distribution of the materials was measured by nitrogen adsorption on a Micrometrics Tristar 3000, according to BET, BJH and T-plot theory. All samples were vacuum dried at 250 °C for 24 h prior to analysis. Thermogravimetric analysis (TGA) was performed to measure the carbon content of the samples using a Netzsch STA 449C Jupiter thermo analyser. The materials were heated to 850 °C in synthetic air (30 ml min^{-1}) at a heating rate of 10 °C min^{-1}. The morphology of the samples was further studied by electron microscopy. 3D information was gathered on a Zeiss Supra 55 VP field emission electron microscope. Furthermore, high magnification micrographs were recorded using a double Cs corrected cold field emission gun JEOL JEM-ARM200F (scanning) transmission electron microscope ((S)TEM). Samples for microscopy investigations were dispersed in EtOH and sonicated for 20 min. A small droplet of the powder/alcohol suspension was placed on a FE-SEM sample holder or an amorphous carbon coated Cu TEM grid, respectively.

Electrochemical characterisation

The electrochemical properties of the prepared LMS cathode materials were assessed by galvanostatic charge–discharge measurements on a Maccor 4200. All measurements were performed at room temperature. The applied potential window and *C* rate are given in the corresponding sections. For a more comparable charge rate *C*, the

Table 1. Sample index of the 4 different samples synthesised in this study.

Sample index	Nominal composition	Flame pyrolysis solution
LMS @ EtOH	Li_2MnSiO_4	80 ml EtOH 20 ml H_2O
LMS @ Xylene	Li_2MnSiO_4	100 ml EtOH 25 ml p-Xylene
LM0.94S @ Xylene	$Li_2Mn_{0.94}SiO_4$	100 ml EtOH 25 ml p-Xylene
LM0.91S @ Xylene	$Li_2Mn_{0.91}SiO_4$	100 ml EtOH 25 ml p-Xylene

theoretical capacity of the exchange of one Li per formula unit was taken into account. For mathematical simplicity the charge rate was defined as a current density of 160 mA $g^{-1} = 1C$. CR2016 coin cells were assembled in a glove box (dry Ar atmosphere) using a 16 mm circular LMS cathode, a circular Li disc as the anode and a Celgard 2400 film as the electrode separator. Commercial 1 M $LiPF_6$ dissolved in a 1:1 volume ratio of ethylene carbonate / diethyl carbonate solution (Aldrich Battery grade) was used as the electrolyte. Additionally, the structural changes of LMS were investigated by *in situ* XRD experiments during the first two galvanostatic cycles. A conventional pouch cell was assembled for *in situ* experiments. The electrodes, separator and electrolyte were the same as previously described. An image of the experimental setup and a description of the *in situ* pouch cells are shown in the supplementary information (stacks.iop.org/TMR/3/025001/mmedia). The cell was galvanostatically cycled on a Princeton Applied Research Parstat 4000 at *C*/16 rate starting from OCP. The potential window was 1.5–4.7 V and the cell was cycled twice. The *in situ* XRD patterns were recorded continuously on a Bruker D 8 Advance Da-Vinci with a LynxEye Xe detector working in Bragg–Brentano ($\Theta/2\Theta$) geometry using Mo K_α radiation in transmission mode. Scans were recorded from 11.7 to 15.8° 2Θ (step-size of 0.015°, integration time 3 s). The *in situ* measurement is presented as a level plot. Due to the additional layers of Al, PE and Li that the beam had to penetrate in transition mode, the observable 2Θ region without interference from the cell components was limited to the abovementioned 2Θ values. Furthermore, pre- and post-*ex situ* analysis scans of the cathode were recorded from 15 to 75° 2Θ (step-size of 0.013°, integration time 1 s) using Cu K_α radiation.

Results and discussion

Structural evolution

All as-pyrolysed powders consisted of a mixture of crystalline Li_2CO_3 and Li–Mn oxides. Si containing oxides could not be detected by XRD and were probably present in an amorphous state. The lack of LMS phase formation during pyrolysis was expected due to the extremely short residence time of the particles in the temperature zone. Further, the oxidising conditions of the CH_4/O_2 flame caused Mn oxidation and thus hindered phase formation. An XRD pattern of the as-pyrolysed powder is given in the supplementary information. The as-pyrolysed samples were then mixed with 25 wt.% corn-starch as a carbon source. Amongst other studies, we previously demonstrated that uncoated LMS has a very low electrochemical activity and thus any characterisation of uncoated LMS samples was omitted in this study [24]. The powder–corn-starch mixture was then heat treated at 550, 600 and 650 °C with a dwell time of 10 h in flowing 5% H_2 95% Ar. Figure 1 shows the corresponding XRD patterns of LMS @ EtOH and LMS @ Xylene.

The crystalline fraction of samples heat treated at 550 °C consisted mainly of different Mn oxides while Li- and Si-containing compounds remained amorphous. The onset of phase formation was, in both cases, detected for samples heat treated at 600 °C and the main phase was, in both cases, dominant at 650 °C. In the case of LMS @ EtOH, traces of MnO and Li_2SiO_3 were detectable, while for LMS @ Xylene, only traces of MnO were detected. But in both cases the main pattern could be clearly attributed to orthorhombic $Pmn2_1$ LMS [6]. Reported higher heat treatment temperatures (700–800 °C) often result in a mixture of $Pmn2_1$ and *Pmnb* LMS. This is clearly recognisable from the appearance of a peak at about 30.6° under Cu K_α radiation, which is sometimes disregarded or misinterpreted as a secondary phase [27, 29, 30]. To prevent this polymorph mixture we limited the heat treatment temperature to 650 °C. In addition, the influence of the dwell time was investigated for the LMS @ Xylene sample. Shorter dwell times resulted in incomplete phase formation, saturation was observed at about 8–10 h, thus all further samples were prepared using these heat treatment parameters. The corresponding figure is shown in the supplementary information. Morphological investigations presented in the next chapter show LMS @ Xylene to be more promising, thus further improvements and characterisation were carried out. As shown in figure 1(b) there are still traces of MnO present next to the main phase. According to preliminary refinements, about 3 wt.% of the phase fraction can be attributed to MnO. This could imply that the synthesised LMS @ Xylene is present in a Mn deficient form. We hence attempted to produce nominal sub stoichiometric LMS @ Xylene, namely LM0.94S @ Xylene and LM0.91S @ Xylene by subsequently reducing the $Mn(NO_3)_2 \bullet 4H_2O$ precursor by 6 and 9 mole%. Figure 2(a) shows the resulting evolution of the MnO secondary phase. Figure 2(b) shows a full pattern refinement of LM0.94S @ Xylene which gave the highest phase purity. The refinement model matches the observed pattern fairly well. The increased background at low 2Θ angles is caused by the fixed slit set up. The calculated crystalline phase fractions and the calculated crystallite size of all samples are summarised in table 2. It should be considered

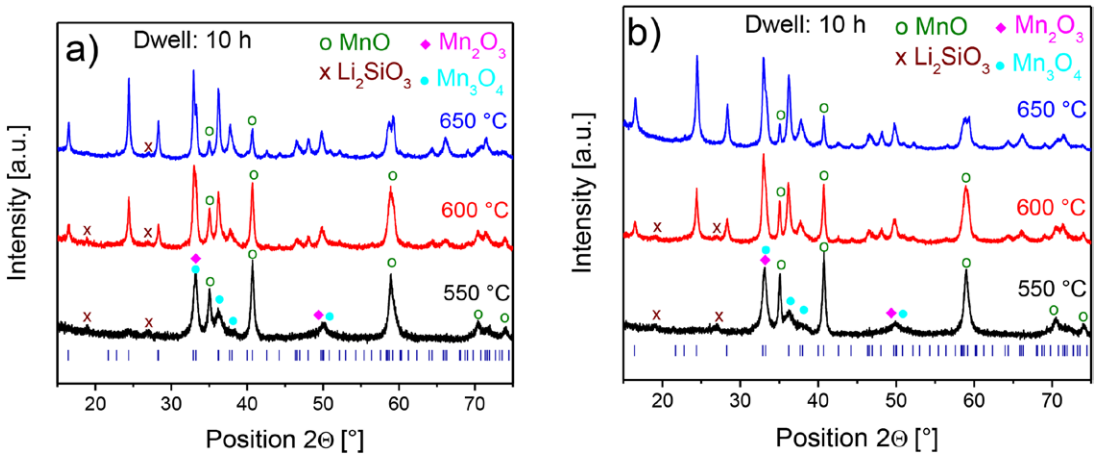

Figure 1. Powder XRD pattern of (a) LMS @ EtOH heat treated at 550, 600 and 650 °C and (b) LMS @ Xylene heat treated at 550, 600 and 650 °C, including denotation of secondary phases and LMS *Pmn2₁* Bragg reflections.

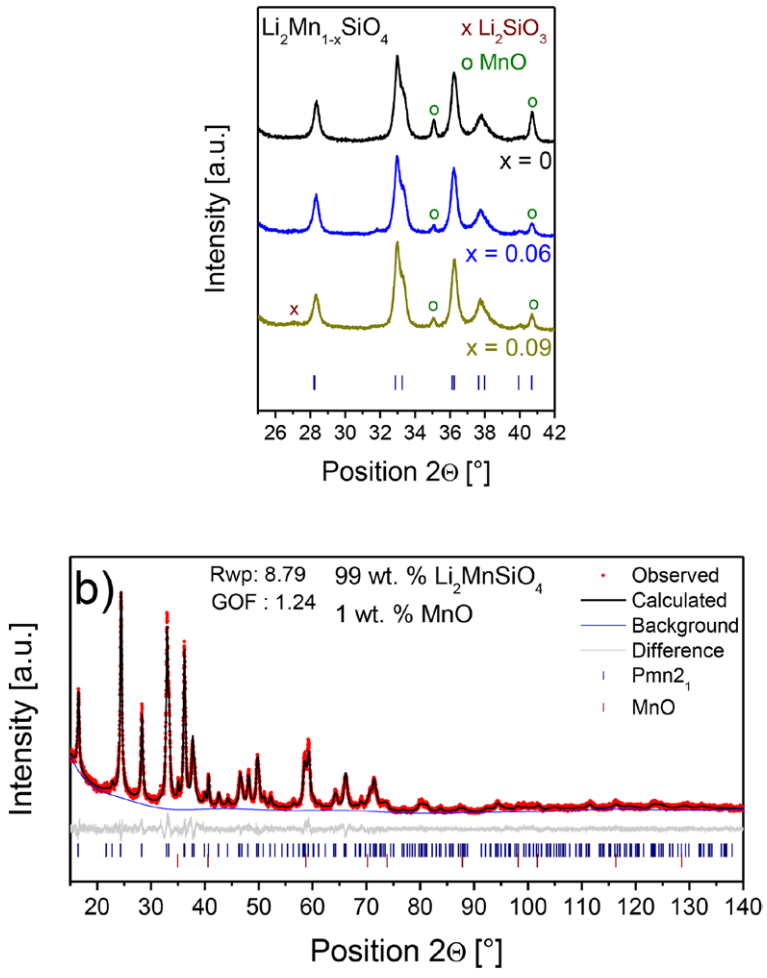

Figure 2. (a) XRD patterns of LMS @ Xylene, LM0.94S @ Xylene and LM0.91S @ Xylene showing the phase evolution of the MnO secondary phase. (b) Full pattern refinement of LM0.94S @ Xylene.

that the error of crystalline quantifications might be as large as 5%, but the significant decrease in peak intensity of the MnO phase strengthens the reliability of the values.

The lattice parameters of the refined orthorhombic *Pmn2₁* structure of LM0.94S @ Xylene are $a = 6.313$ Å, $b = 5.383$ Å and $c = 4.970$ Å. The lattice parameters of the other two compositions synthesised by Xylene-assisted FSP are very similar and they all agree with data from the literature [6]. Figure 2(a) and table 2 show that the MnO secondary phase is reduced but does not disappear even at 9 mole% Mn sub-stoichiometry. For the stoichiometric and 6 mole% Mn sub-stoichiometric samples MnO was the only detectable secondary phase, but when the Mn

Table 2. Phase fractions of LMS @ Xylene, LM0.94S @ Xylene and LM0.91S @ Xylene according to Rietveld refinements.

Sample index	Li_2MnSiO_4 (wt.%)	MnO (wt.%)	Li_2SiO_3 (wt.%)	Crystallite size from XRD (nm)
LMS @ Xylene	97	3	—	23.5
LM0.94S @ Xylene	99	1	—	24
LM0.91S @ Xylene	96.5	1.5	2	25

Table 3. Surface area and carbon content of synthesised LMS samples.

Sample index	BET surface area ($m^2\ g^{-1}$)	External surface area ($m^2\ g^{-1}$)	Micropore area ($m^2\ g^{-1}$)	Carbon content (wt.%)
LMS @ EtOH	72.2	49.2	23.0	6
LMS @ Xylene	97.3	67.8	29.5	6
LM0.94S @ Xylene	93.5	64	29.5	6
LM0.91S @ Xylene	88.7	61.4	27.3	6

concentration is further reduced, Li_2SiO_3 emerges and no further reduction of the MnO phase is observed. This could be caused by only a small difference in energy of formation of MnO and LMS and the tolerance of LMS for Mn deficiency resulting in a low driving force for phase combination at the given temperature. In fact, the appearance of MnO as the only visible secondary phase, even for samples with reduced Mn content, indicates that LMS samples synthesised in this study are Mn deficient. The amount of MnO at 6% and 9% Mn sub-stoichiometry is low, but relatively comparable, and hence strengthens the conclusion. This could be charge compensated either by vacancies in the oxygen sub-lattice or by a partial oxidation of Mn^{2+} to Mn^{3+} to maintain electro-neutrality. It is noteworthy that all refinements underestimate the Mn 2a occupancy to values about 0.7–0.75 without showing high values of Li/Mn site reversal. Mn^{2+} on a Li-site would cause changes in the diffraction pattern due to the much higher electron density. On the other hand, it could hardly be distinguished whether a Mn site is actually vacant or occupied by Li due to the very low electron density of Li^+. Dominko *et al* explained this phenomenon with disorder [6]. Some of the Mn atoms could occupy states in the interstitial octahedral voids. This would explain the remaining mismatch between the observed and the calculated XRD patterns and the underestimated Mn occupancy. Further details of all refinements are shown in the supplementary information.

Influence of precursor solution combustibility and final heat treatment on the powder morphology

The precursor solution, or in other words the fuel for the FSP process, had a major impact on the morphology of the final powders. Since LMS shows rather poor electronic and ionic conductivities, the particle size is very important for the electrochemical properties. Furthermore, porosity in the meso and macro range is beneficial to maximise the contact area of the cathode material and the electrolyte and thus enhance the electrochemical kinetics. Table 3 shows the surface area values divided into the micropore area and external surface area and the residual carbon content of the sample measured by TGA. We define the external area by the part of the total BET surface area that is not attributed to microporosity, which is by definition smaller than 2 nm in diameter. We have previously shown that to a great extent the micropore area can be attributed to porosity in the amorphous carbon coating [24].

All LMS samples showed a very similar carbon content of about 6 wt.%. Further, all Xylene-assisted FSP samples showed 20–30% larger external surface areas compared to the LMS @ EtOH sample. SEM analysis revealed major morphological differences between samples produced with and without Xylene addition. Figure 3 shows SEM micrographs of LMS @ EtOH and LMS @ Xylene, where (a) and (c) show the corresponding powders as received from FSP and (b) and (d) the final powders of LMS @ EtOH and LMS @ Xylene, respectively. The carbon former hinders exaggerated particle growth during heat treatment and the nanoparticles prepared by the FSP process remain preserved after the powders were heat treated and carbon coated [24]. Both powders consist of porously agglomerated nanograins but the as-pyrolysed and final powder of LMS @ EtOH exhibited a large number of dense spherical particles in the sub-μm and μm regime. These particles were also present in the LMS @ Xylene sample but in a much lower quantity. The appearance of spherical dense particles during conventional spray pyrolysis is well known and caused by volume precipitation during pyrolysis [31]. The reduced density of these spherical sub-μm particles can be directly linked to the combustibility of the precursor solution, which in case of the EtOH/p-Xylene solution is enhanced compared to the EtOH/H_2O solution. A similar phenomenon was observed by Dahl *et al* during the comparison of different solvents used for FSP of binary oxides [32].

TEM/STEM analysis further revealed that the LMS @ Xylene sample consists of nanoparticles with a mean particle size of about 20 nm ranging from 10 to 40 nm. For this analysis the remaining few spherical sub-μm particles were omitted. This fits well with the calculated crystallite size from XRD data. Bright-field TEM and

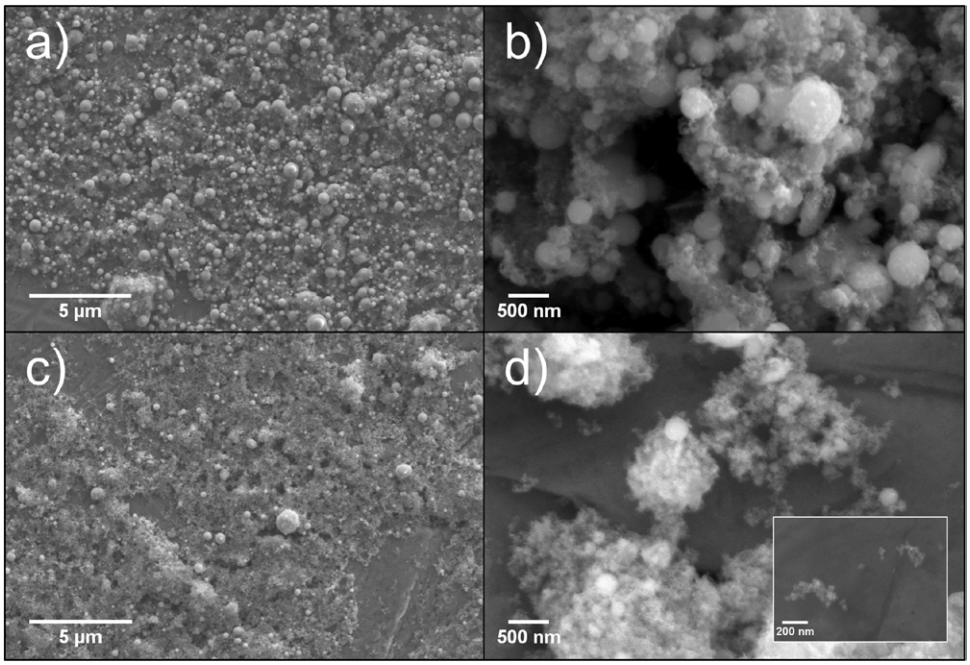

Figure 3. SEM micrographs of different LMS powders, magnifications are given in brackets. (a) LMS @ EtOH as-pyrolysed (5k), (b) LMS @ EtOH (20k), (c) LMS @ Xylene as-pyrolysed (5k), (d) LMS @ Xylene (20k) the inset show the same powder at a higher magnification (40k).

STEM images are given in figure 4. In the STEM micrograph the amorphous carbon layer surrounding the grains and the crystal orientation are also indicated.

The impact of precursor combustibility on the electrochemical performance

As mentioned in the previous section, the precursor solution combustibility resulted in quite noticeable morphological changes. Large micron-sized particles or dense agglomerates in the same range are undesirable for materials offering low ionic and electronic conductivity values like LMS. To verify the influence of the morphology, cathodes were fabricated from all synthesised LMS powders and galvanostatically cycled in a potential window of 1.5–4.7 V at room temperature and *C*/16 rate. Figure 5(a) shows the corresponding first and second cycle. The corresponding differential capacities of LMS @ Xylene are shown in figure 5(b).

All samples suffered from an irreversible capacity loss (ICL) of about 30% in the first cycle. This loss can partly be attributed to parasitic oxidation reactions of the electrolyte and interphase formation but also the structural degradation must be considered. The structure may already completely collapse during the first oxidation and does not allow full relithiation upon reduction. Despite the ICL, which is present in all cases, a tremendous increase in discharge capacity of over 100% from 80 to about 170 mAh g^{-1} is visible when comparing LMS @ EtOH with the Xylene-assisted samples. In the Mn sub-stoichiometry series almost no difference in discharge capacity was detectable, which is probably due to comparable phase purity and the fact that all synthesised samples showed a Mn stoichiometry <1 according to XRD data. The second charge profile looks completely different from the first one, which indicates structural changes. This behaviour is well known and understood for Li_2FeSiO_4, where the delithiation is shifted to lower potentials caused by structural rearrangements [33–36]. In contrast, not only is the onset of oxidation lowered, but the slope of the charge curve is also much steeper without any plateau-like regions, which could be explained by the loss of crystallinity and thus order. The discharge profile in the second cycle remains the same but a loss in discharge capacity of about 10–15 mAh g^{-1} is observed. The differential capacity curves resemble this behaviour and are in agreement with cyclic voltammetry studies and differential capacity studies in the literature [21, 23, 37–39]. Upon the first anodic polarisation, which mainly corresponds to the Mn^{2+}/Mn^{3+} oxidation, only a single asymmetric peak is observed. Muraliganth *et al* claim the peak to corresponds to both the Mn^{2+}/Mn^{3+} and Mn^{3+}/Mn^{4+} redox couples [21]. Whether that is the case, or the second oxidation is hidden in the asymmetry on the right hand side of the peak, cannot be concluded. The first cathodic polarisation shows two broad peaks. The first minor peak, only visible as a shoulder, is located at about 3.9 V. The main signal peaks at about 3 V. The splitting into two extremely broad peaks is related to the structural degradation. The chemical environment of a cation has a huge influence on its redox potential. In this case, the shoulder at higher potentials is believed to correspond to Mn still in its initial coordination, whereas the main peak at lower potential shows Mn in an altered environment. The onset of oxidation upon the second anodic polarisation is lowered to 2.8 V. Furthermore, do the structural changes cause an extremely broad peak which does not allow for conclusions if it is

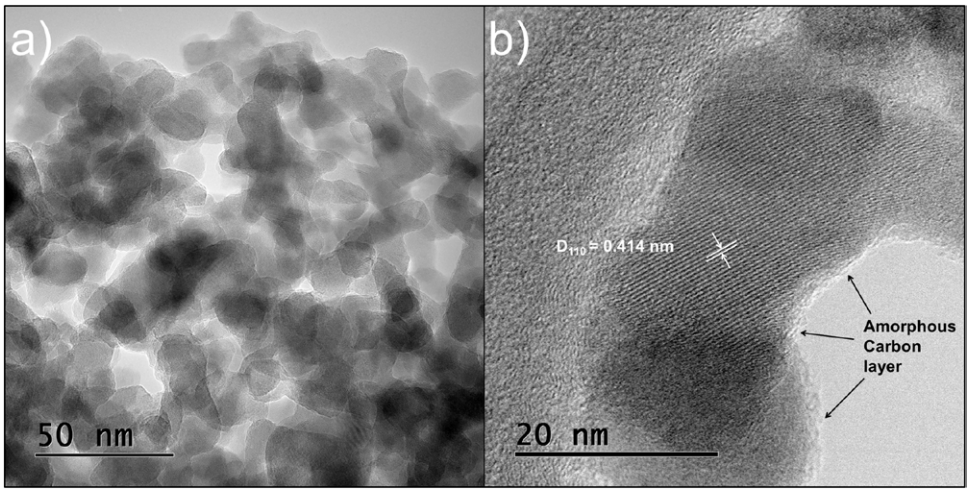

Figure 4. (a) TEM micrograph showing porously agglomerated LMS grains. (b) STEM micrograph of LMS grains surrounded by a thin layer of amorphous carbon. Note: the amorphous structure on the left side of the micrograph in (b) is the TEM sample grid.

attributable to one or two redox couples? The second cathodic polarisation resembles the first cycles with a slight decrease in the overall signal. This fade in capacity makes it more challenging to investigate the rate capability since the discharge capacity is influenced by both the number of cycles the battery was tested for and the charge rate. Figure 6(a) shows the first discharge capacity of LM0.94S @ Xylene at four different rates ranging from *C*/50 to *C*/2. The coulombic efficiency is in all cases about 70%. The inset shows the first 20 cycles of the same materials at *C* rates from *C*/2 to 5C. Furthermore, the capacity fade with respect to the potential window, and thus the amount of Li extracted/inserted for 150 cycles, is shown in figure 6(b).

Figure 6(a) shows the first discharge capacity rating from 145 to 190 mAh g^{-1} depending on the *C* rate. The values at *C*/50 and *C*/16 are 190 and 170 mAh g^{-1}, respectively. Additionally, it has to be considered that capacities reported here are with respect to the LMS/C where the amorphous carbon coating acts as conductivity enhancer. To obtain the specific capacity of the bare silicate the weight of the carbon coating (6 wt.%) needs to be subtracted which leads to values of ~180 and 200 mAh g^{-1} at *C*/16 and *C*/50, respectively. Both values cannot be solely attributed to the $Mn^{3+/}Mn^{2+}$ redox couple, especially considering that the charge capacity is 30% higher. It is believed that the second Li is mobilised to a certain amount at slow *C* rates by the Mn^{4+}/Mn^{3+} redox couple. Figure 6(b) shows the known capacity decay of LMS to be directly related to the potential window of operation and thus to the amount of Li being extracted from the structure during each charge. LM0.94S @ Xylene was cycled in two different potential windows, 1.5–4.7 and 2–4.4 V at *C*/4. The sample cycled in the large potential window showed an initial discharge capacity of 156 mAh g^{-1}. After 20 cycles the capacity dropped to 58 mAh g^{-1}, which corresponds to capacity retention of only 37% On the other hand, the sample cycled in the smaller potential window retained 62% of its initial value of 112 mAh g^{-1}. It can be concluded that the capacity decay is directly linked to the amount of Li removed from the structure and thus the oxidation state of Mn. To further confirm that the ICL in the first cycle cannot be solely attributed to unwanted oxidation reactions, we attempted to completely mobilise the first Li at lower potentials. This was accomplished by inserting a potentiostatic step in the galvanostatic cycling program. LM0.91S @ Xylene was charged at *C*/16 to a moderate potential of 4.2 V and kept at this potential until the current density dropped to a value of 0.005 *C*. Afterwards it was discharged at *C*/16 to 1.5 V and subsequently cycled again without the potentiostatic step. The result of the experiment is shown in figure 7.

The charge capacity of 163 mAh g^{-1} fits well with the theoretical capacity of the one-electron reaction, especially considering the carbon coating and the fact that the studied LMS samples show slight Mn sub-stoichiometry. The corresponding discharge capacity was only 134 mAh g^{-1}, hence still showing a prominent ICL of 18% even at potentials well within the kinetically controlled stability range of the electrolyte [40]. In order to further confirm that the capacity decay is caused by irreversible amorphisation, the structural evolution of LM0.94S @ Xylene was monitored during the first two galvanostatic cycles in a pouch cell by *in situ* x-ray diffraction using Mo K_α radiation in transmission mode. The corresponding *in situ* level plot is shown in figure 8. The 2Θ range was limited to 11.7–15.8°. In this range the (1 1 1) (2 0 0) and (2 1 0) (0 2 0) double peaks were monitored. Under Cu K_α radiation the corresponding peaks are located at 28.3° and 33° 2Θ. The intensity of these two double peaks during the first scan was set as maximum intensity in the level plot representation. This short scan range was chosen to omit strong peaks from the polyethylene and Al from the pouch material and current collector. To keep a good time resolution the scan, the time was chosen to be as short as possible (~22 min) while the cell was charged at a low rate of *C*/16. The charge–discharge behaviour in the pouch cell was somewhat different to the experiments on coin-cells

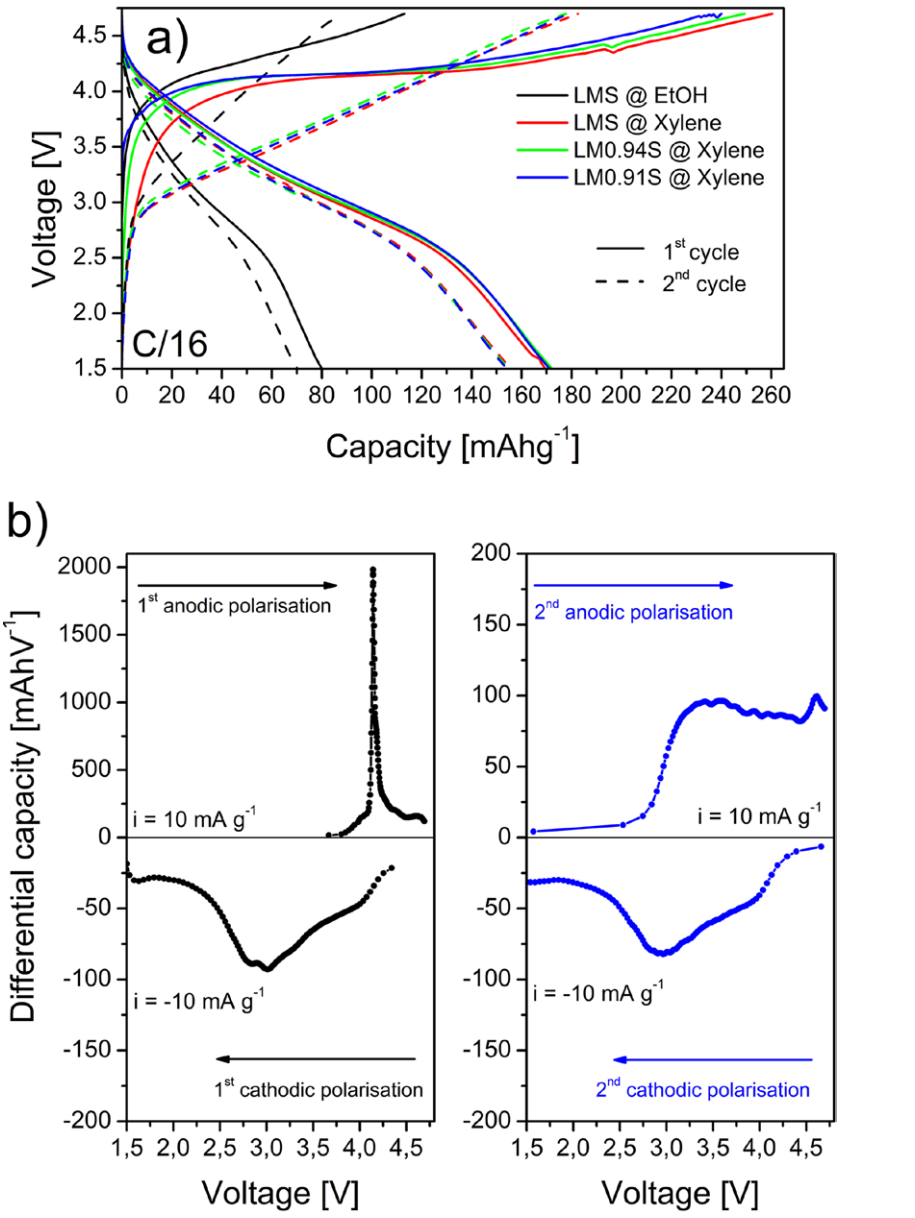

Figure 5. (a) First and second galvanostatic cycle of LMS @ EtOH, LMS @ Xylene, LM0.94S @ Xylene and LM0.91S @ Xylene. (b) Differential capacity during the first two cycles of LMS @ Xylene. Note the different scale during the first anodic polarisation.

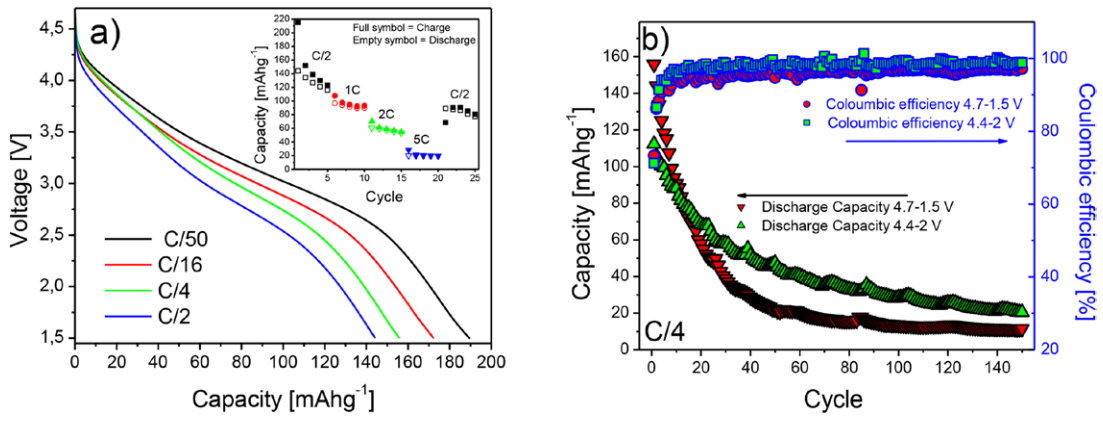

Figure 6. (a) First discharge of LM0.94S @ Xylene at different rates; 20 cycles at higher rates are shown in the figure inset. (b) Discharge capacity of LM0.94S @ Xylene during 150 cycles in two different potential windows 4.7–1.5 and 4.4–2.0 V. The (blue) right ordinate shows the coulombic efficiency in %.

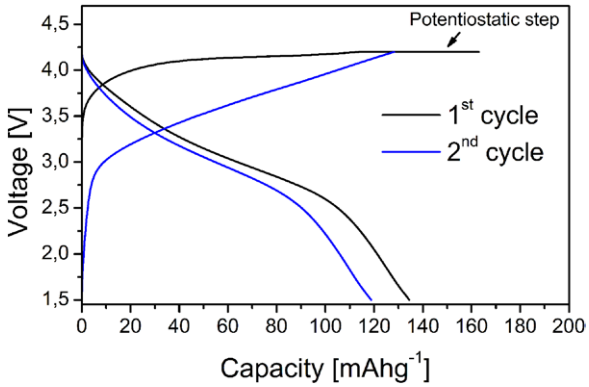

Figure 7. First two cycles of LM0.91S @ Xylene at *C*/16 in a potential window of 1.5–4.2 V including a potentiostatic step at 4.2 V until the current density declined to a value of 0.005 *C* at the end of the first charge.

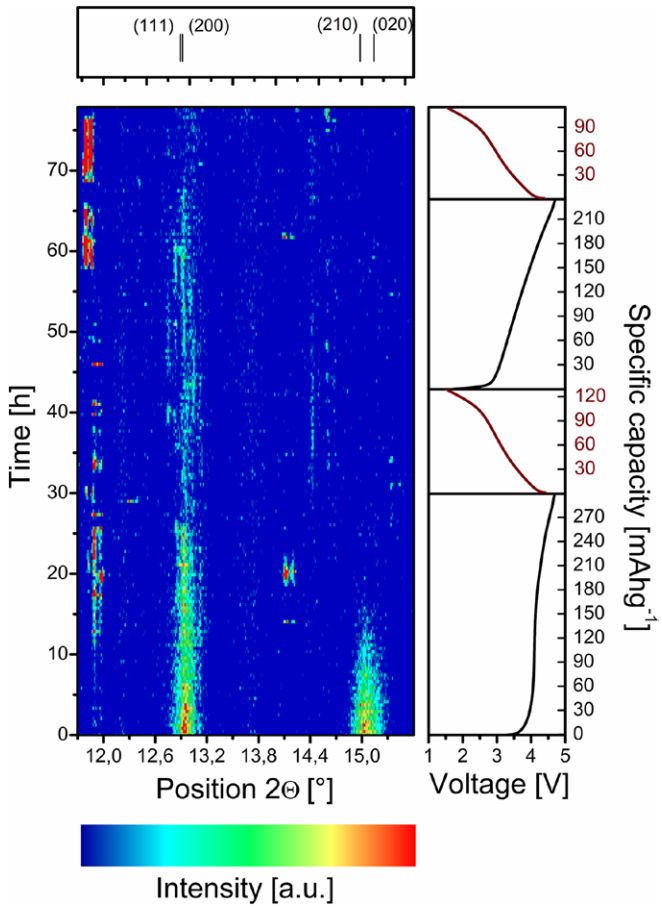

Figure 8. *In situ* XRD level plot during the first two galvanostatic cycles at *C*/16 of an LM0.94S @ Xylene pouch cell using Mo K_α radiation in transmission mode. At the top, the two observed double peaks are shown and on the right is the cycling profile.

showing an increased charge and a decreased discharge capacity which could be caused by parasitic side reactions due to an inhomogeneous pressure distribution in our *in situ* cells [41].

The *in situ* XRD level plot shows clearly the loss of crystallinity of the LM0.94S @ Xylene cathode during the first charge. The (2 1 0) (0 2 0) double peak disappears at potentials slightly higher than 4 V and a state of charge of about 120 mAh g^{-1} which corresponds to 0.72 Li per formula unit if side reactions are excluded. The (1 1 1) (2 0 0) double peak diminishes into the background noise at higher potentials of about 4.6 V. During discharge, and in the subsequent cycle, none of the $Pmn2_1$ peaks reappear; we thus conclude that the amorphisation is irreversible. Interestingly, other peaks appear in the *in situ* measurement. As shown in the level plot, one sharp double peak or two very close peaks appear at about 11.8–11.9° 2Θ and they seem to be slightly shifted to lower 2Θ angles in

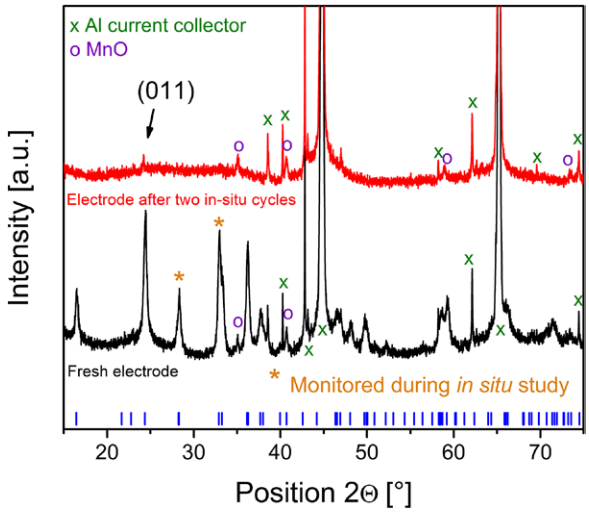

Figure 9. XRD patterns of an LM0.94S @ Xylene fresh electrode and after two *in situ* cycles. The peaks monitored during the *in situ* study are denoted by an asterisk. LMS $Pmn2_1$ Bragg reflections are added and the peaks originating from the MnO impurity and the Al current collector are denoted. Additional Al peaks are instruments caused by parasitic Cu Kβ and W L radiation.

the second cycle. Another peak appears in both the first and second charge at potentials of around 4.25 V at 2Θ of about 14.1° but disappears again as the potential is increased. Unfortunately, due to the short scan range and the quality of data none of these peaks could be indexed. Also, one has to consider that any crystallisation occurring in the cell would be monitored since the experiment was performed in transmission mode. To further investigate changes on the cathode and to gain a better signal to noise ratio, the *in situ* cell was disassembled and the cathode was washed multiple times with DEC to remove $LiPF_6$. A diffractogram was recorded from 15 to 75° 2Θ using Cu K_α radiation. The results are compared to a fresh electrode and shown in figure 9.

None of the observed unknown peaks during the *in situ* measurement were observed on the cycled electrode, making it impossible to conclude the chemical composition of the observed crystallisation and the exact place where it occurs. Alongside the peaks of the Al current collector and the MnO secondary phase, only a weak signal which could be attributed to the (0 1 1) main peak of $Pmn2_1$ LMS is still visible while all other peaks of the main structure completely disappeared, confirming the irreversible amorphisation of LMS upon cycling.

Conclusions

With liquid-feed flame spray pyrolysis and subsequent post processing, an alternative method which enables preparation of nanoscale LMS/C in large quantities is reported. It was shown that the combustibility of the precursor solution had a major impact on the particle morphology and the resulting electrochemical performance. All prepared samples based on the 5:1 EtOH/P-Xylene solution are believed to exhibit slight Mn sub-stoichiometry. For the nominal and the 6 mole% Mn sub-stoichiometric samples, traces of MnO were the only detectable secondary phase. Further reduction of the Mn concentration caused formation of Li_2SiO_3. The highest capacity achieved in this study was 190 mAh g^{-1} during the first discharge at a charge rate of *C*/50. At a higher *C* rate of *C*/2, the first discharge capacity still exceeded 140 mAh g^{-1}. Values over 166 mAh g^{-1} cannot solely be caused by the $Mn^{2+/3+}$ redox couple. Also, the high charge capacities suggest activity of the second redox couple ($Mn^{3+/4+}$) at slow *C* rates, but the structural collapse does not allow full relithiation during the discharge. The theoretical capacity was not reached even during the charge at low rates, and it can thus be concluded that, to mobilise the second Li ion, not only must the structural instability be overcome, but also electrolytes with a larger potential window are required. All samples in this study showed a prominent irreversible capacity loss between the first charge and discharge and capacity fade caused by the structural instability of LMS. *In situ* XRD experiments showed that a complete loss of crystallinity already occurs during the first charge. This loss was shown to be irreversible and no XRD peaks corresponding to LMS reoccurred during the discharge and the subsequent cycle. It is concluded that LMS has major shortcomings to be solved before it could potentially become interesting for battery applications, since the ability of delivering two Li per formula unit is not possible in the given potential range without the stabilisation of the structure. Nonetheless, it is noteworthy that in principle the reported synthesis should also be applicable for Li_2FeSiO_4 which shows more potential as a stable low cost cathode material for Li-ion batteries, as well as other transition metal oxides suitable for battery applications.

Acknowledgments

The research council of Norway is gratefully acknowledged for funding the SilicatBatt project (grant number: 216469/E20). NORTEM seed and competence projects (grant number 11) and Dr Per Erik Vullum are acknowledged for TEM analysis.

References

[1] Tarascon J M and Armand M 2001 Issues and challenges facing rechargeable lithium batteries *Nature* **414** 359–67
[2] Gaines L and Cuenca R 2000 *Costs of Lithium-Ion Batteries for Vehicles Annual Report* vol 48 (Argonne National Laboratory) (http://www.anl.gov/energy-systems/publication/costs-lithium-ion-batteries-vehicles)
[3] Wood D L, Li J and Daniel C 2015 Prospects for reducing the processing cost of lithium ion batteries *J. Power Sources* **275** 234–42
[4] Padhi A K, Nanjundaswamy K S and Goodenough J B 1997 Phospho-olivines as positive-electrode materials for rechargeable lithium batteries *J. Electrochem. Soc.* **144** 1188
[5] Nytén A, Abouimrane A, Armand M, Gustafsson T and Thomas J O 2005 Electrochemical performance of Li_2FeSiO_4 as a new Li-battery cathode material *Electrochem. Commun.* **7** 156–60
[6] Dominko R *et al* 2006 Structure and electrochemical performance of Li_2MnSiO_4 and Li_2FeSiO_4 as potential Li-battery cathode materials *Electrochem. Commun.* **8** 217–22
[7] Kuganathan N and Islam M S 2009 Li_2MnSiO_4 lithium battery material: atomic-scale study of defects, lithium mobility, and trivalent dopants *Chem. Mater.* **21** 5196–202
[8] Andre D *et al* 2015 Future generations of cathode materials: an automotive industry perspective *J. Mater. Chem.* A **3** 6709–32
[9] Dominko R 2008 Li_2MSiO_4 (M = Fe and/or Mn) cathode materials *J. Power Sources* **184** 462–8
[10] Politaev V V, Petrenko A A, Nalbandyan V B, Medvedev B S and Shvetsova E S 2007 Crystal structure, phase relations and electrochemical properties of monoclinic Li_2MnSiO_4 *J. Solid State Chem.* **180** 1045–50
[11] Duncan H *et al* 2011 Novel Pn polymorph for Li_2MnSiO_4 and its electrochemical activity as a cathode material in Li-ion batteries *Chem. Mater.* **23** 5446–56
[12] Gummow R J, Sharma N, Peterson V K and He Y 2012 Crystal chemistry of the Pmnb polymorph of Li_2MnSiO_4 *J. Solid State Chem.* **188** 32–7
[13] Islam M S *et al* 2011 Silicate cathodes for lithium batteries: alternatives to phosphates? *J. Mater. Chem.* **21** 9811–8
[14] Gummow R J and He Y 2014 Recent progress in the development of Li_2MnSiO_4 cathode materials *J. Power Sources* **253** 315–31
[15] Larsson P, Ahuja R, Liivat A and Thomas J O 2010 Structural and electrochemical aspects of Mn substitution into Li_2FeSiO_4 from DFT calculations *Comput. Mater. Sci.* **47** 678–84
[16] Saracibar A, Wang Z, Carroll K J, Meng Y S and Dompablo M E A 2015 New insights into the electrochemical performance of Li_2MnSiO_4 : effect of cationic substitutions *J. Mater. Chem.* A **3** 6004–11
[17] Dominko R, Bele M, Kokalj A, Gaberscek M and Jamnik J 2007 Li_2MnSiO_4 as a potential Li-battery cathode material *J. Power Sources* **174** 457–61
[18] Dominko R, Arčon I, Kodre A, Hanžel D and Gaberšček M 2009 *In situ* XAS study on Li_2MnSiO_4 and Li_2FeSiO_4 cathode materials *J. Power Sources* **189** 51–8
[19] Qu L, Fang S, Yang L and Hirano S 2014 Synthesis and characterization of high capacity Li_2MnSiO_4/C cathode material for lithium-ion battery *J. Power Sources* **252** 169–75
[20] Rangappa D, Murukanahally K D, Tomai T, Unemoto A and Honma I 2012 Ultrathin nanosheets of Li_2MSiO_4(M = Fe, Mn) as high-capacity Li-ion battery electrode *Nano Lett.* **2012** 1146–51
[21] Muraliganth T, Stroukoff K R and Manthiram A 2010 Microwave-solvothermal synthesis of nanostructured Li_2MSiO_4/C(M = Mn and Fe) cathodes for lithium-ion batteries *Chem. Mater.* **22** 5754–61
[22] Kempaiah D M, Rangappa D and Honma I 2012 Controlled synthesis of nanocrystalline Li_2MnSiO_4 particles for high capacity cathode application in lithium-ion batteries *Chem. Commun.* **48** 2698
[23] Świętosławski M, Molenda M, Furczoń K and Dziembaj R 2013 Nanocomposite C/Li_2MnSiO_4 cathode material for lithium ion batteries *J. Power Sources* **244** 510–4
[24] Wagner N, Svensson A-M and Vullum-Bruer F 2015 Effect of carbon content and annealing atmosphere on phase purity and morphology of Li_2MnSiO_4 synthesized by a PVA assisted sol–gel method *Solid State Ion.* **276** 26–32
[25] Sun D *et al* 2013 *In situ* synthesis of carbon coated Li_2MnSiO_4 nanoparticles with high rate performance *J. Power Sources* **242** 865–71
[26] Liu W, Xu Y and Yang R 2010 Synthesis and electrochemical properties of Li_2MnSiO_4/C nanoparticles via polyol process *Rare Met.* **29** 511–4
[27] Aravindan V *et al* 2011 Influence of carbon towards improved lithium storage properties of Li_2MnSiO_4 cathodes *J. Mater. Chem.* **21** 2470
[28] Pratsinis S E 1998 Flame aerosol synthesis of ceramic powders *Prog. Energy Combust. Sci.* **24** 197–219
[29] Devaraj S, Kuezma M, Ng C T and Balaya P 2013 Sol–gel derived nanostructured Li_2MnSiO_4/C cathode with high storage capacity *Electrochim. Acta* **102** 290–8
[30] Shao B and Taniguchi I 2013 Synthesis of Li_2MnSiO_4/C nanocomposites for lithium battery cathode employing sucrose as carbon source *Electrochim. Acta* **128** 156–62
[31] Messing G L, Zhang S-C and Jayanthi G V 1993 Ceramic powder synthesis by spray pyrolysis *J. Am. Ceram. Soc.* **76** 2707–26
[32] Dahl P I *et al* 2015 Flame spray pyrolysis of electrode materials for energy applications *Materials Research Society Symp. Proc.* vol 1747
[33] Nytén A, Kamali S, Häggström L, Gustafsson T and Thomas J O 2006 The lithium extraction/insertion mechanism in Li_2FeSiO_4 *J. Mater. Chem.* **16** 2266
[34] Sirisopanaporn C, Masquelier C, Bruce P G, Armstrong A R and Dominko R 2011 Dependence of Li_2FeSiO_4 electrochemistry on structure *J. Am. Chem. Soc.* **133** 1263–5
[35] Liivat A 2012 Structural changes on cycling Li_2FeSiO_4 polymorphs from DFT calculations *Solid State Ion.* **228** 19–24
[36] Zhou H, Einarsrud M A and Vullum-Bruer F 2013 *In situ* x-ray diffraction and electrochemical impedance spectroscopy of a nanoporous Li_2FeSiO_4/C cathode during the initial charge/discharge cycle of a Li-ion battery *J. Power Sources* **238** 478–84
[37] Wang H *et al* 2014 Lithium deficient mesoporous $Li_{2-x}MnSiO_4$ with significantly improved electrochemical performance *J. Power Sources* **247** 497–502
[38] Wang M, Yang M, Ma L, Shen X and Zhang X 2014 Structural evolution and electrochemical performance of Li_2MnSiO_4/C nanocomposite as cathode material for Li-ion batteries *J. Nanomater.* **2014** 1–6

[39] Bhaskar A, Deepa M, Rao T N and Varadaraju U V 2012 *In situ* carbon coated Li_2MnSiO_4/C composites as cathodes for enhanced performance Li-ion batteries *J. Electrochem. Soc.* **159** A1954–60
[40] Scrosati B and Garche J 2010 Lithium batteries: status, prospects and future *J. Power Sources* **195** 2419–30
[41] Villevieille C, Sasaki T and Novák P 2014 Novel electrochemical cell designed for operando techniques and impedance studies *RSC Adv.* **4** 6782

Nils Wagner received his BSc in 2010 and MSc 2012 both in chemical engineering from FH Muenster University of Applied Sciences. He received his PhD in March 2016 in Material Science and Engineering at NTNU and is currently a post doc at the same department.

Ann Mari Svesson received her MSc from the Department of Physics (NTNU) in 1993 and in 1997 she was awarded her PhD from the Department of Electrochemistry (NTNU). She has held several positions in SINTEF, where she was Research Manager in the Energy Conversion Group in the years 2005 to 2011, and parts of that period from 2007 on she was also a Senior Scientist at SITNEF Materials and Chemistry. Since 2012 Svensson has been a professor at the department of Materials Science and Engineering at NTNU.

Fride Vullum-Bruer received her MSc in 2002 and PhD in 2005, both in Chemical Engineering from The University of Tulsa (USA). From January 2006 until September 2008 she was a post doctoral fellow at The Department of Materials Science and Engineering (NTNU) and was appointed Associate Professor at the same department in September 2008 where she is currently employed. Vullum-Bruer has worked in research on Li-ion batteries since about 2002,